

1 **Bursts of fast propagating swarms of induced earthquakes at the Groningen gas field**

2 Krittanon Sirorattanakul¹, John D. Wilding¹, Mateo Acosta¹, Yuexin Li¹, Zachary E. Ross¹,
3 Stephen J. Bourne², Jan van Elk³, and Jean-Philippe Avouac^{1,4}

4 ¹ Division of Geological and Planetary Sciences, California Institute of Technology, 1200 E.
5 California Blvd., Pasadena, CA, 91125 USA

6 ² Shell Global Solutions International B.V., Grasweg 39, 1031 HW, Amsterdam, The Netherlands

7 ³ Nederlandse Aardolie Maatschappij B.V., Schepersmaat 2, 9405 TA, Assen, The Netherlands

8 ⁴ Department of Mechanical and Civil Engineering, California Institute of Technology, 1200 E.
9 California Blvd., Pasadena, CA, 91125 USA

10 Corresponding author: Krittanon Sirorattanakul (ksirorat@caltech.edu)

11 **Abstract**

12 Gas extraction from the Groningen gas reservoir, located in northeastern Netherlands, has led to a
13 drop in pressure driving compaction and induced seismicity. Stress-based models have shown
14 success in forecasting induced seismicity in this particular context and elsewhere, but they
15 generally assume that earthquake clustering is negligible. To assess earthquake clustering at
16 Groningen, we generate an enhanced seismicity catalog using a deep-learning-based workflow.
17 We identify and locate 1369 events between 2015 and 2022, including 660 newly detected events
18 not previously identified by the standard catalog from the Royal Netherlands Meteorological
19 Institute. Using the nearest-neighbor distance approach, we find that 72% of events are background
20 independent events, while the remaining 28% belong to clusters. 55% of the clustered events are

21 swarm-like, while the rest are aftershock-like. Among the swarms include five newly identified
22 swarm sequences propagating at high velocities between 3 – 50 km/day along directions that do
23 not follow mapped faults or existing structures and frequently exhibit a sharp turn in the middle of
24 the sequence. The swarms occurred around the time of the maximum compaction rate between
25 November 2016 and May 2017 in the Zechstein layer, above the anhydrite caprock, and well-
26 above the directly induced earthquakes that occur within the reservoir and caprock. We suggest
27 that these swarms are related to aseismic deformation within the salt formation rather than fluids.
28 This study suggests that propagating swarms do not always signify fluid migration.

29 **Introduction**

30 Industrial activities, such as gas extraction, wastewater disposal, hydraulic stimulation, geothermal
31 energy production, carbon dioxide sequestration, and water impoundment from dams can produce
32 substantial stress changes in the Earth's crust that can induce seismicity (Ellsworth, 2013; Grigoli
33 *et al.*, 2017; Keranen and Weingarten, 2018; Atkinson *et al.*, 2020; Wu *et al.*, 2022; Moein *et al.*,
34 2023). The induced earthquakes can occasionally reach magnitudes of 5 or above, with
35 hypocenters that are often shallower than those of natural seismicity (Hough, 2015), making it
36 capable of damaging nearby structures (Clayton *et al.*, 2016). Management of seismic risks to be
37 within an acceptable level is critical for successful operations.

38 Induced earthquakes, which exclude background earthquakes driven by tectonics and other natural
39 causes of stress changes, can generally be grouped into two modes based on their clustering
40 behaviors. The first mode includes independent background events that are driven directly by the
41 stress changes due to the large scale human activity, whether from changes in pore pressure as the
42 fluid diffuses (Hubbert and Rubey, 1959; Nur and Booker, 1972) or long-range poroelastic stress
43 changes (Segall, 1989; Segall *et al.*, 1994; Goebel *et al.*, 2017; Zhai *et al.*, 2019). These events are
44 expected to follow a Poisson process, generally non-homogeneous, with time-varying rates
45 governed by stress changes (Dempsey and Suckale, 2017; Dahm and Hainzl, 2022; Smith *et al.*,
46 2022; Acosta *et al.*, 2023). The second mode includes the clustered events that appear close in
47 space and time with some independent events and often occur as aftershocks, or more occasionally
48 as foreshocks as observed for natural seismicity as well (Ogata, 1988). Mechanistically, these
49 events are triggered by stress changes imparted by a previous earthquake rather than the industrial
50 operations. Aftershocks generally follow well-known patterns, including the decay of their
51 occurrence rates with time as a power law (Omori, 1894; Utsu, 1961) and a scaling in which the

52 largest aftershock is approximately 1.2 magnitude unit lower than the mainshock (Richter, 1958).
53 Clustered events may occasionally deviate from this well-defined pattern and occur as enigmatic
54 bursts of small-magnitude earthquakes without an identifiable mainshock, referred to as swarms
55 (Mogi, 1963). They often exhibit migratory patterns (Audin *et al.*, 2002; Hainzl and Fischer, 2002;
56 Chen and Shearer, 2011) and are a manifestation of underlying aseismic processes such as
57 spontaneous slow slip events (Lohman and McGuire, 2007; Passarelli *et al.*, 2015; Gualandi *et al.*,
58 2017; Jiang *et al.*, 2022), fluid pressure diffusion (Shapiro *et al.*, 1997; Audin *et al.*, 2002; Hainzl
59 and Fischer, 2002; Shelly *et al.*, 2013; Ruhl *et al.*, 2016; Ross and Cochran, 2021), or a complex
60 interaction of both (Dublanchet and De Barros, 2021; Sirorattanakul *et al.*, 2022; Yukutake *et al.*,
61 2022). Clustering is generally small in induced seismicity with a proportion of clustered events
62 generally less than 30% (Zaliapin and Ben-Zion, 2016; Cochran *et al.*, 2020; Karimi and Davidsen,
63 2023), while clusters typically represent up to 70% of natural seismicity (Zaliapin and Ben-Zion,
64 2013a). Swarms have also been observed in the context of induced seismicity where they are
65 generally ascribed to fluid migration (Ake *et al.*, 2005; Baisch *et al.*, 2006; Albaric *et al.*, 2014;
66 Kwiatek *et al.*, 2019).

67 In this study, we take advantage of publicly available seismic datasets related to seismicity induced
68 by production in the Groningen gas field in the northeastern Netherlands (Dost *et al.*, 2017;
69 Willacy *et al.*, 2019; Oates *et al.*, 2022) to investigate the degree of clustering and the possible
70 mechanisms involved. We produce an enhanced seismicity catalog for the region using a deep-
71 learning-based workflow. The improved catalog reveals many previously unidentified events,
72 which enables more extensive statistical analysis of earthquake clusters. The newly detected events
73 include five distinct swarm sequences propagating at high velocity between 3 – 50 km/day.

75 **The Groningen gas field, overview of previous studies of induced seismicity**

76 The Groningen gas field is the largest in Western Europe (Figure 1), with an initial gas reserve of
77 approximately 2913 billion cubic meters (BCM) (Burkitov *et al.*, 2016). The gas comprises 85%
78 methane (CH₄), 14% nitrogen (N₂), and 1% carbon dioxide (CO₂) (Stäuble and Milius, 1970;
79 Burkitov *et al.*, 2016). The reservoir lies at a depth of between 2.6 and 3.2 km and spans
80 approximately 35 km east-west and 50 km north-south as a part of the Upper Rottingend Group
81 composed of interbedded Slochteren sandstone and Ten Boer claystone units. Its thickness varies
82 substantially from 90 m in the southeast to 300 m in the northwest. The coal layers in the
83 underlying Pennsylvanian Carboniferous limestone are the source of the gas. The reservoir is
84 sealed by an overlying thick and impermeable caprock of anhydrite and evaporite layers of the
85 Permian Zechstein group, an aquifer toward the north, and a system of normal faults (de Jager and
86 Visser, 2017). Because of the limited connection with the surrounding groundwater, gas extraction
87 has led to significant pressure depletion from 34.68 MPa, close to hydrostatic pressure (Burkitov
88 *et al.*, 2016), to < 10 MPa (Meyer *et al.*, 2023), which resulted in surface subsidence of almost 40
89 cm (Smith *et al.*, 2019).

90 While the field has been in production since 1963, induced seismicity did not start until 1991 (Dost
91 *et al.*, 2017). From 1991 to 2013, the number of earthquakes increased exponentially, prompting
92 significant efforts to deploy additional monitoring instruments. The first regional network in
93 operation since 1995 consisted of eight stations, each with three-component geophones at four
94 different depth levels (50 m, 100 m, 150 m, and 200 m) and a surface accelerometer. Several
95 upgrades of the network followed. In a major upgrade late 2014, 59 additional stations were
96 deployed, significantly improving seismic activity detection (Dost *et al.*, 2017). Most earthquakes
97 align well with one of the > 1100 normal faults mapped by seismic techniques that offset the gas

98 reservoir (Visser and Solano Viota, 2017) and are located primarily within the reservoir (Willacy
99 et al., 2019) or in the overburden (Smith *et al.*, 2020). They are thought to be driven primarily by
100 poroelastic stresses induced by bulk reservoir volume decrease (Bourne *et al.*, 2014; Dempsey and
101 Suckale, 2017; Candela *et al.*, 2019; Smith *et al.*, 2022) or by stress concentration around faults
102 offsetting the reservoir resulting from compaction (Bourne *et al.*, 2014; Buijze *et al.*, 2017; Van
103 Wees *et al.*, 2018). The largest earthquake to date is the 2012 M_w 3.6 Huizinge earthquake, which
104 sparked public concerns and prompted the regulators to request ramping down of production and
105 to eventually shut it down long before exhaustion of the gas reserve (de Waal *et al.*, 2015; van
106 Thienen-Visser and Breunese, 2015; Muntendam-Bos *et al.*, 2017).

107 In recent years, many researchers have developed computationally efficient models to forecast
108 occurrence rates of induced seismicity based on stress changes from industrial operations (Segall
109 and Lu, 2015; Bourne and Oates, 2017; Dempsey and Suckale, 2017; Bourne *et al.*, 2018;
110 Langenbruch *et al.*, 2018; Candela *et al.*, 2019, 2022; Zhai *et al.*, 2019; Richter *et al.*, 2020; Dahm
111 and Hainzl, 2022; Heimisson *et al.*, 2022; Kühn *et al.*, 2022; Smith *et al.*, 2022; Acosta *et al.*,
112 2023; Kim and Avouac, 2023). One major limitation of these stress-based models is that they do
113 not account for interactions between earthquakes that may lead to secondary triggering and appear
114 as clustered events. While induced earthquakes tend to have fewer clustered events than natural
115 earthquakes, their proportions can be $> 50\%$ depending on the geological settings, which is non-
116 negligible (Zaliapin and Ben-Zion, 2016). A better understanding of clustering behaviors of
117 induced seismicity can lead to further improvements in these models.

118

119 **Data and Methods**

120 *Enhanced seismicity catalog generation*

121 The Royal Netherlands Meteorological Institute (KNMI) has been the authoritative governmental
122 institution responsible for maintaining a seismicity catalog for the area surrounding the Groningen
123 gas field since 1995. To supplement the KNMI catalog, we use a recently developed deep-learning-
124 based workflow to build an enhanced high-resolution seismicity catalog between 2015 and 2022
125 covering the domain spanning latitude $53.05 - 53.50^{\circ}\text{N}$ and longitude $6.48 - 7.05^{\circ}\text{E}$. As
126 summarized below, the workflow consists of multiple steps, including phase picking, phase
127 association, earthquake location, and magnitude estimation.

128 Waveform data from seismic stations in the NL and NR networks located within our domain are
129 used in this analysis (Figure S1). We first apply the PhaseNet automated phase picking algorithm
130 based on a convolutional neural network (Zhu and Beroza, 2019) to detect P- and S-wave arrivals.
131 The algorithm accepts one- or three-component waveform data as input and outputs a list of
132 timestamped P- or S-wave arrival times. We use the standard model included with the PhaseNet
133 distribution, which was trained on California data based on manual picks from seismic analysts at
134 the Northern California Earthquake Data Center but has been shown to effectively generalize to
135 other regions worldwide, including Hawaii (Wilding *et al.*, 2023), Italy (Tan *et al.*, 2021), and
136 Arkansas, USA (Park *et al.*, 2020). The initial iteration of the catalog, spanning from mid-2015 to
137 2018, includes picking from both surface and borehole seismometers. However, when we expand
138 the catalog to include the first few months of 2015 and from 2019 to 2022, we only apply PhaseNet
139 to surface sensors for computational efficiency. Additionally, for instruments with a sampling rate
140 greater than 100 Hz, we decimate waveform data to 100 Hz per PhaseNet requirements. The output

141 from PhaseNet also has probability labels between 0 and 1, indicating confidence in the pick. We
142 set a probability threshold of 0.3 and remove picks below this confidence threshold.

143 The P and S arrival picks are then associated into discrete earthquake events using the Gaussian
144 Mixture Model Associator, GaMMA (Zhu *et al.*, 2022). GaMMA probabilistically assigns clusters
145 of P and S picks to individual sources based on identified hyperbolic moveouts and iterates those
146 assignments using the expectation-maximization process. The main parameters controlling the
147 association process are the maximum time ε between two picks to be considered as a neighbor of
148 the other and the scalar P- and S-wave velocity used to backproject arrivals. Even though GaMMA
149 uses a uniform velocity model, it can account for travel-time errors in back-projection due to three-
150 dimensional variation of the velocity model by allowing large uncertainty in arrival times during
151 the clustering stage. We test different parameters and identify the best set of parameters as those
152 that include the greatest number of events previously identified by KNMI. The best combination
153 of parameters uses ε of 3 seconds, a P-wave velocity of 3.0 km/s, and an S-wave velocity of 1.8
154 km/s. With this set of parameters, GaMMA identifies 709 out of 739 events in the KNMI catalog
155 over the same spatial and temporal coverage. After the association, we filter out previously
156 unidentified events with fewer than 5 P or S picks and are left with 2591 events. Finally, we
157 manually inspect waveforms of all newly identified events and remove the spurious picks resulting
158 in 1369 events, including 660 newly detected events (Figure S2 and S3).

159 The events are then located with a modified version of the Hypocenter inversion with Stein
160 Variational Inference and physics-informed neural networks (HypoSVI) program (Smith *et al.*,
161 2021), adapted to allow for a 3-D velocity model. The velocity model of the Groningen region
162 used in this study was produced by Nederlandse Aardolie Maatschappij (NAM) from seismic
163 reflection, seismic refraction, sonic log and well core samples (Nederlandse Aardolie

164 Maatschappij, 2017). Since HypoSVI inverts for the full posterior distribution of an earthquake
165 location, the algorithm also outputs associated location uncertainties. Compared with the KNMI
166 catalog, we find approximately 40 mismatched events. Most of these events are located near the
167 edges of the velocity model domain by both our algorithm and by KNMI. They are most likely
168 affected by the low number of picks on stations within the velocity model domain and increased
169 picking errors for arrivals with a lower signal-to-noise ratio. To maintain the integrity of the
170 catalog, we manually assign the locations of these events to those provided by KNMI, which can
171 be identified by their depth of exactly 3 km. The events that include the borehole picks can be
172 distinguished by event ID numbers that begin with “100” in contrast to other events that only have
173 picks on surface geophones. Events with picks only from the surface geophones have larger depth
174 uncertainty, as evidenced by several surface-sensor-only events with depths far from the reservoir.
175 These depths can be considered artifacts of the data downsampling process. We have also
176 compared the epicentral (horizontal) locations derived using picks from all sensors and only from
177 surface sensors. They are largely unaffected by excluding the picks from the borehole sensors.
178 Local earthquake magnitudes (M_L) are calculated with the same procedure used by KNMI
179 (NORSAR, 2018), which can be calculated by using the following equation:

$$M_L = \log_{10} A + 1.33 \log_{10} R + 0.00139R + 0.424 \quad (1)$$

180 where A is amplitude measurement in mm on a simulated Wood-Anderson seismometer of the
181 deepest available borehole sensor for a given station, and R is the source-receiver distance in km.
182 The amplitudes are measured as the peak signal amplitude of the waveform (absolute value). While
183 it is possible to convert local magnitude to moment magnitude using the relation derived by Dost
184 *et al.* (2018), we restrict our analysis to local magnitude.

185 *Clustering analysis*

186 To analyze the clustering behaviors of seismicity in the Groningen gas field, we apply the nearest-
187 neighbor distance approach (Zaliapin and Ben-Zion, 2013a, 2013b) to the enhanced seismicity
188 catalog. We consider only events located within the boundary of the Groningen gas field that are
189 larger than the completeness magnitude (M_c) of 0.5. For each event j in the catalog, we search for
190 the preceding event i that is most likely to be the parent (mainshock) of event j . The proximity
191 distance between any event pair (i, j) can be quantified using a space-time-magnitude metric
192 normalized by the magnitude of the parent event (Baiesi and Paczuski, 2004; Zaliapin *et al.*, 2008)
193 defined as follows:

$$\eta_{ij} = t_{ij} (r_{ij})^{d_f} 10^{-b(m_i - M_c)} \quad (2)$$

194 where $t_{ij} = t_j - t_i$ is the time between the event pair, r_{ij} is the distance between the epicenters of
195 the event pair, d_f is the fractal dimension of earthquake epicenters taken to be 1.6 (Zaliapin and
196 Ben-Zion, 2013a), b is the Gutenberg-Richter b-value of the frequency-magnitude distribution,
197 and m_i is the magnitude of event i . Since depth uncertainty is large, we do not include depths in
198 the proximity distance calculations.

199 For each event j , the event i^* with the smallest proximity distance η_{ij} is the nearest neighbor and
200 hence most likely to be the parent of event j . The results can be expanded to two dimensions as
201 rescaled time T_j and rescaled distance R_j , defined as follows (Zaliapin and Ben-Zion, 2013a):

$$T_j = t_{i^*j} 10^{-\frac{b}{2}(m_{i^*} - M_c)} \quad (3)$$

$$R_j = (r_{i^*j})^{d_f} 10^{-\frac{b}{2}(m_{i^*} - M_c)}$$

202 The distribution of nearest-neighbor distance η_j is expected to be bimodal. The first mode is the
203 independent events represented by a time-stationary, space-inhomogeneous Poisson process
204 concentrating along $\log_{10} T_j + \log_{10} R_j = \text{constant}$. The second mode is the clustered events with
205 considerably smaller T_j and R_j , constituting foreshock-mainshock-aftershock sequences and
206 swarms (Zaliapin *et al.*, 2008; Zaliapin and Ben-Zion, 2013a). The separation between the two
207 modes can be approximated by a 1-D Gaussian mixture model applied on η_j (Hicks, 2011) using
208 Matlab *fitgmdist* function. The mode separator η_0 is chosen to be where the probability density
209 function of the two modes intersects. We consider events with $\eta_j \geq \eta_0$ to be independent events
210 and $\eta_j < \eta_0$ to be clustered events (Zaliapin and Ben-Zion, 2013a).

211 The nearest-neighbor distance approach was originally analyzed for an epidemic-type aftershock
212 sequence (ETAS) model (Ogata, 1988) with an assumption that the background independent
213 events follow a time-stationary, space-inhomogeneous Poisson process (Zaliapin *et al.*, 2008). In
214 the case of induced seismicity, we expect the background Poisson rates of independent events to
215 be inhomogeneous in time as modulated by injection or extraction rates. To test *a posteriori* the
216 effectiveness of the nearest-neighbor distance approach for induced seismicity and the robustness
217 of the estimated mode separator η_0 , we take events with $\eta_j \geq \eta_0$, create 100 shuffled catalogs by
218 randomly permuting the order of the magnitudes and locations, and calculate nearest-neighbor
219 distances for events in these shuffled catalogs, similar to those done in Karimi and Davidsen
220 (2023). Since the shuffling removes any clusters while preserving the seismicity rate and spatial
221 distribution, the distribution of nearest-neighbor distances of these shuffled events reflects the true
222 distribution of the independent mode and hence the majority of events should have $\eta_{j,\text{shuffled}} \geq \eta_0$

223 if the chosen η_0 is appropriate. Unlike in Karimi and Davidsen (2023), by shuffling only events
224 with $\eta_j \geq \eta_0$, we reduce bias of the clustered events on the temporal rate of independent events.

225 In principle, we can also completely remove the time clustering by sampling new times from a
226 uniform distribution (Zaliapin and Ben-Zion, 2020) but then we would also remove any time-
227 inhomogeneous nature of the independent events.

228 Furthermore, we also evaluate the relative variability of the interevent times distribution using the
229 coefficient of variation (CoV), defined as the ratio of its standard deviation and its mean. Random
230 process (Poissonian) is expected to have CoV in order of unity. Larger CoV suggests the presence
231 of clustering, while smaller CoV suggests a periodic behavior. For a given η_0 , the CoV can be
232 used to evaluate whether the independent events are Poissonian. If the chosen η_0 is too small,
233 events with $\eta_j \geq \eta_0$ would include some clustered events and hence the CoV would become
234 significantly greater than one. In contrary to the shuffling analysis which evaluates the upper bound
235 of the appropriate η_0 , the CoV evaluates its lower bound.

236 We additionally use the Schuster spectrum method (Ader and Avouac, 2013) to verify that, once
237 clustered events are removed based on the chosen value of the mode separator η_0 , the remaining
238 events are consistence with a non-homogeneous Poisson process. The method is based on the
239 Schuster tests (Schuster, 1897), which evaluates the amount of seismicity rate variation for a given
240 periodicity. By calculating the Schuster p-value for different periods, we construct a Schuster
241 spectrum and compare with the expectation for a Poisson process. This procedure aids in
242 verification of the quality of the declustering.

243 To further study the relationship between events, we create a spanning tree by connecting each
244 event to its most likely parent. The strength of each link is inversely proportional to the nearest-
245 neighbor distance η_j . By removing weak links with $\eta_j \geq \eta_0$, we create a spanning forest consisting

246 of single-event trees with no links and other multievent clusters (Zaliapin and Ben-Zion, 2013a).
247 The independent events previously identified include the singles and the first event from each
248 cluster. We can calculate the average leaf depth for each cluster by averaging the number of links
249 needed to connect events without children to the first event or the root (Zaliapin and Ben-Zion,
250 2013b). Swarm-like sequences have large average leaf depth, while foreshock-mainshock-
251 aftershock sequences have small average leaf depth.

252

253 **Results**

254 *Catalog overall properties*

255 Compared to the standard catalog from the Royal Netherlands Meteorological Institute (KNMI),
256 our deep-learning-based workflow enables us to increase the number of detected events between
257 2015 and 2022 from 739 to 1369. 709 events from the KNMI catalog were identified by our
258 workflow, leaving only 30 events unidentified by our method. 1297 events are located within the
259 horizontal extent of the gas field, which we use for the analysis hereafter.

260 Despite being automatically generated products, our events display good agreement in both
261 locations and magnitudes with the KNMI catalog (Figure S4). The horizontal location differences
262 for events with $M_L \geq 0.5$ are less than 675 m on average. Most events with large location
263 differences are either located near the edge of the available velocity model or small magnitude
264 events where arrival picks have large uncertainty. The magnitude differences are less than 0.1
265 magnitude unit on average. Only 78 events (12%) have magnitude differences greater than 0.2
266 magnitude units. There is one M3 event that is presented in our catalog but not in the KNMI
267 catalog. Since that event is located close the edge of the velocity model, the arrival picks may have

268 large uncertainty and bias its location, and therefore, its magnitude. Our catalog also reports depth
269 rather than a fixed depth of 3 km, as the KNMI catalog does. In comparison to the catalog by
270 Willacy *et al.* (2019), which utilizes full-waveform inversion to determine the event location, the
271 horizontal location differences for events with $M_L \geq 0.5$ decrease slightly to a mean value of 563
272 m (Figure S5). We have refined the depth determination by including time picks from the borehole
273 sensors for the time spanning mid-2015 to 2018, during which we observed a concentration of
274 swarms as detailed below.

275 The increase in detection is consistent across the period studied. Many new detections are related
276 to small events with signals close to the noise floor. However, a significant portion of new
277 detections are the five bursts of small-magnitude (M_L 0.5 – 1.5) swarm-like sequences that double
278 the earthquake rates between November 2016 and May 2017 (Figure 2a), which we discuss further
279 in the “Swarm sequences” Section. Our catalog has the completeness magnitude (M_c) of 0.5
280 estimated using the maximum curvature method (Wiemer and Wyss, 2000). Here, we do not use
281 the typical correction factor of 0.2 (Woessner and Wiemer, 2005), because it is advantageous to
282 keep more events for the statistical analysis. The b-value slope of the frequency magnitude
283 distribution is determined to be 0.86 by applying the B-Positive method (van der Elst, 2021) to all
284 events with a conservative minimum magnitude difference of 0.2 (Figure 2b). Note that the B-
285 Positive method does not require a complete catalog. With these additional events, the enhanced
286 catalog can unlock new insights into the clustering behaviors of earthquakes in the Groningen gas
287 field.

288

289 *Clustering behaviors*

290 The nearest-neighbor distance approach is applied to 726 earthquake epicenters in the enhanced
291 catalog with $M_L \geq 0.5$. The distribution of nearest-neighbor distance η_j expanded in the form of
292 rescaled time T_j and rescaled distance R_j is shown in Figure 3a. By fitting η_j with a 1-D Gaussian
293 mixture model, we find the best-fit mode separator of $\log_{10} \eta_0 = -3.05$. We find that 522 events
294 (72%) are independent, while the remaining 204 events (28%) appear to be clustered (Figure 3b).

295 The two-dimensional probability distribution of nearest-neighbor distances of the 100 shuffled
296 catalogs are averaged and shown in Figure 3c. Since the rate of independent events vary only
297 gradually during this period, their distribution similarly concentrates along a line with $\log_{10} T_j +$
298 $\log_{10} R_j = \text{constant}$ with almost all reshuffled events (93%) having $\eta_j \geq \eta_0$, validating the
299 approach and the chosen mode separator. The results are qualitatively similar if the earthquake
300 hypocenters are used instead of the epicenters, accounting also for the depths (Figure S6).
301 Furthermore, the independent events (those with $\eta_j \geq \eta_0$) have CoV of approximately one,
302 consistent with them being Poissonian. If we were to choose $\eta_0 < -4$, events with $\eta_j \geq \eta_0$ include
303 clusters as CoV becomes significantly greater than one (Figure S7).

304 The Schuster spectrum calculated for the non-declustered catalog shows low p-values, lower than
305 expected for a Poisson process, which drifts to even lower value starting at a period of about 2-3
306 days (Figure S8a). This pattern shows that the catalog contains clusters (Ader and Avouac, 2013)
307 and we can infer they have durations of a few days or eventually longer. However, if we use only
308 the independent events, the drifting low p-values disappear (Figure S8b), further validating the
309 choice of the value of the mode separator chosen.

310 We proceed to analyze the spatiotemporal evolution of the events from each of the two modes
311 (Figure 4). The independent events align well with mapped faults and have the seismicity rate that
312 is gradually changing with time. On the other hand, the clustered events show multiple lineations
313 that do not align with mapped faults and occur as short-duration bursts of events in time. The most
314 prominent clusters are the five bursts of small magnitude (M_L 0.5 – 1.5) swarm-like sequences
315 occurring between November 2016 and May 2017. The others appear to be aftershocks of the
316 larger $M_L > 2$ events. By construct, if a sequence has a foreshock, the mainshock will be identified
317 as a clustered event rather than an independent event because the foreshock would be its parent,
318 which explains why some of the larger events are identified as clustered.

319 The spanning tree created by connecting each event with its nearest neighbor if $\eta_j < \eta_0$ reveals
320 448 single-event clusters (62% of events) and 73 multievent clusters (38% of events). Their
321 detailed statistics are shown in Figure 5. The average size of the multievent clusters is 3.8 events
322 with a standard deviation of 3.6 events. The large standard deviation reflects significant variations
323 in clustering behaviors. All earthquakes with $M_L > 2.5$ are a part of multievent clusters, with the
324 number of events in the cluster growing with mainshock magnitude. On average, the largest
325 aftershock is 1.5 magnitude unit lower than the mainshock, in line with those expected from Båth's
326 law (Richter, 1958). The average leaf depth of these aftershock sequences is 1.3, indicating that
327 most of the events are triggered by the mainshock rather than being aftershocks of aftershocks. On
328 the other end of the spectrum, there are multievent clusters that exist as swarm-like sequences
329 without a clearly identifiable mainshock ($M_{\text{mainshock}} - M_{\text{largest aftershock}} \ll 1$, contradicting
330 Båth's law) and a larger value of average leaf depth (d_{leaf}) of up to 8.7. For an earthquake sequence
331 with an average of two aftershocks for each earthquake, the cluster size (n_{clust}) would then be
332 $2^{d_{\text{leaf}}}$. Therefore, this motivates using d_{leaf} of $\log_2 n_{\text{clust}}$ as a cutoff for binary classification

333 between swarm-like and aftershock-like clusters. Considering only clusters with at least 5 events,
334 we find 7 swarm-like clusters ($d_{\text{leaf}} \geq \log_2 n_{\text{clust}}$) with a total of 77 events (55% of clustered
335 events) and 9 aftershock-like clusters ($d_{\text{leaf}} < \log_2 n_{\text{clust}}$) with a total of 64 events (45% of
336 clustered events). The analysis suggests that the clustered events are slightly dominated by swarm-
337 like sequences. Among the aftershock-like clusters, the events are 16% foreshocks, 14%
338 mainshocks, and 70% aftershocks.

339

340 *Swarm sequences*

341 There were five noticeable swarm-like clusters between November 2016 and May 2017, each
342 lasting 1 to 5 days and consisting of 10 to 20 events, with M_L ranging from 0.66 to 1.56 (Figure
343 6). Outside of this period, we did not find any other noticeable swarm clusters. Upon further
344 investigation of their kinematics, all swarms migrate with velocities ranging from 3 to 50 km/day.
345 We numbered the swarms from 1 to 5 based on the order that they occurred. The migration
346 occurred along one single direction for swarms 1 and 2 and two different orthogonal directions for
347 swarms 3 – 5. For swarms 3 and 4, there exists also ~ 15 hour pauses with no events before the
348 migration direction switches. The migration directions do not follow mapped faults or other known
349 features of the reservoir. While there are not enough events to determine the exact shape of the
350 migration front, it is possible to model them with $\sqrt{4\pi Dt}$ where D would be an apparent hydraulic
351 diffusivity, and t is time. In the case of fluid-driven swarms, the fitted D would be related to the
352 hydraulic diffusivity of the fault zones (Shapiro *et al.*, 1997), though with a conversion factor that
353 accounts for the time delays associated with earthquake nucleation (Kim and Avouac, 2023). The
354 swarms in our study have D ranging from 70 – 800 m²/s, much larger than a commonly accepted
355 range for fluid-driven swarms of 0.005 – 10 m²/s (Amezawa *et al.*, 2021). In comparison to other

356 swarms around the world, the scaling between migration velocity and duration places them closer
357 to slow-slip events and swarms driven dominantly by slow-slip events than other injection-induced
358 swarms (Danré *et al.*, 2022). We further discuss possible drivers for these swarms in “Possible
359 drivers of swarm-like sequences” Section.

360 Another interesting observation is that the swarms occurred at a depth of between 1.5 to 2.5 km.
361 While there could be some uncertainty with the absolute depth locations, they are certainly located
362 toward the shallower side when compared to other earthquakes that are generally thought to be
363 located near the top of the reservoir (Willacy *et al.*, 2019; Smith *et al.*, 2020). As a result, this
364 would place them in the 1 – 2 km thick Zechstein evaporite (salt) above the anhydrite caprock,
365 well above the gas reservoir (Figure 7).

366

367 **Discussion**

368 *Comparison of clustered fraction with other studies*

369 Induced earthquakes are known to have a lower proportion of clustered events than naturally
370 occurring tectonic earthquakes due to high driving stresses from anthropogenic activities in
371 comparison to tectonic loading (Schoenball *et al.*, 2015; Zaliapin and Ben-Zion, 2016; Cochran *et*
372 *al.*, 2018; Martínez-Garzón *et al.*, 2018). Here, we compile in Table 1 the clustered proportion of
373 seismicity from different regions as reported by previous studies. We find that the clustered events
374 can account for up to 70% of naturally occurring tectonic earthquakes but no more than 30% of
375 induced earthquakes. The estimate of 28% from this study places the Groningen gas field well
376 within the range estimated for other induced seismicity settings. Other studies on the clustered
377 proportion of seismicity from the Groningen gas field provide different estimates of the clustered

378 proportion varying from a few percent up to 27%, which are generally lower than the 28% that we
379 report here (Candela *et al.*, 2019; Muntendam-Bos, 2020; Post *et al.*, 2021; Trampert *et al.*, 2022).
380 Among those that also uses the nearest-neighbor distance approach, Candela *et al.* (2019) finds
381 18% of clustered events between 1993 – 2016, while Muntendam-Bos (2020) finds only 6% of
382 clustered events between 1995 – 2018, but the proportion increases to 22% if consider only the
383 period between 2014 – 2018. On the other hand, Post *et al.* (2021) uses the statistics of the
384 interevent times and finds a larger value of 27% for the clustered proportion. The scatter of the
385 clustered proportion identified by the different studies can be attributed to various factors,
386 including but not limited to: variation of earthquake rates and clustering behaviors with time
387 (Trugman *et al.*, 2016; Martínez-Garzón *et al.*, 2018; Muntendam-Bos, 2020), accuracy of
388 earthquake locations (Muntendam-Bos, 2020), and the five swarm sequences occurring between
389 November 2016 and May 2017 that were not previously identified other seismicity catalogs, and
390 the cutoff magnitude employed (Zaliapin and Ben-Zion, 2013a). By removing the five swarms,
391 our estimate of the clustered proportion becomes 19%, which is almost equivalent to the estimate
392 from Candela *et al.* (2019). We also calculate the clustered proportion using the different cutoff
393 and find that the clustered proportion generally decreases with larger cutoff and becomes stable at
394 between 18 – 20% as the cutoff exceeds M_L of 1.2 at which the five swarm sequences are excluded
395 from the analysis (Figure 8).

396

397 *Possible drivers of swarm-like sequences*

398 Although the migration of swarms in the Groningen gas field can be modeled with a square root
399 of time typically associated with fluid pressure diffusion (Shapiro *et al.*, 1997), it is unlikely that
400 fluid plays any dominant role because of the following reasons. First, the migration direction

401 should be along the maximum spatial pressure gradient, which follows the spatial derivative of the
402 compaction rate. This contradicts the observations in which the migration direction seems to align
403 more along the contours of constant compaction (Figure 9a). Second, the migration velocity is on
404 the order of 10 km/day, which requires a much higher hydraulic diffusivity than the values
405 typically expected for fluid-driven swarms (Amezawa *et al.*, 2021). Third, while fault slip can
406 enhance permeability, allowing for faster diffusion rates, the migration directions do not follow
407 mapped faults or any known structures. There may be other unmapped faults in which the
408 migration follows as there are focal mechanisms with fault planes not orienting along the mapped
409 faults (Willacy *et al.*, 2019). Nevertheless, because the swarms are located in the Zechstein salt
410 well above the impermeable anhydrite caprock that allows the gas to be preserved for millions of
411 years (Figure 7), the faults in the Zechstein layer are probably not hydraulically connected to the
412 reservoir and are most probably located in the anhydrite fragments that are embedded within the
413 Zechstein evaporite rather than in the evaporite itself which cannot support brittle fractures due to
414 its viscous nature. Hence, the swarms cannot be driven by direct fluid contact.

415 Besides fluids, cascading earthquakes can create an apparent diffusive expansion front
416 (Helmstetter and Sornette, 2002). However, the swarms consist of only small M_L 0.5 – 1.5 events
417 which would correspond to a rupture dimension of ~ 15 – 40 m, much smaller than the average
418 distance of ~ 1 km between events (Figure 6). While there could exist a chain of smaller
419 undetectable events that connect the larger ones, this is unlikely as our deep-learning-based
420 workflow should be able to detect some events below M_L 0.5 (Figure 2), but we detect none.
421 Therefore, cascade triggering is also unlikely.

422 These swarms occurred just after the period of accelerated compaction (Figure 9b), suggesting
423 they might be related to the large strain rate from such period that could trigger swarms in the

424 Zechstein layer above the reservoir. However, since the compaction rate seems to be more
425 correlated with the rate of independent events rather than the rates of all events (Figure S9), some
426 additional mechanisms are required to connect compaction to the swarms. While seismic events
427 in the salt are rare because salt is highly ductile they can occur in case of large strain rates, for
428 example related to the collapse of mining cavity (Kinscher *et al.*, 2016) or fault creep (Barnea
429 Cohen *et al.*, 2022), or in relation to fluid injection (Lei *et al.*, 2019). Alternatively, these events
430 could also occurred within the anhydrite fragments embedded in the salt (Spetzler and Dost, 2017).
431 Since there are no mining activities in the Zechstein layer and that the faults in this layer are most
432 probably not hydraulically connected to the reservoir, propagating episodes of aseismic
433 deformation is the most probable mechanism. While there are no detectable geodetic signals in
434 either GPS or InSAR during the time of the swarms, aseismic creep may locate too deep or being
435 too small to be detected. Swarms that are driven by aseismic slip generally propagate at high
436 velocity in the order of km/hr (Lohman and McGuire, 2007; Sirorattanakul *et al.*, 2022), which is
437 consistent with the observations of the Groningen swarms. The aseismic fault creep could occur
438 within the fragments of anhydrite embedded in the Zechstein evaporite. Such creep can be driven
439 by the long-range poroelastic stress changes incurred by pore pressure change in the reservoir.
440 Poroelastic effects are indeed needed to explain both the surface subsidence and the induced
441 seismicity at Groningen and are therefore explicitly included in most models (Bourne *et al.*, 2014;
442 Buijze *et al.*, 2017; Dempsey and Suckale, 2017; Candela *et al.*, 2019; Smith *et al.*, 2022) .
443 Alternatively, aseismic fault creep may be driven by stress induced by bulk creep in the
444 surrounding Zechstein evaporite as the salt redistribute, possibly in response to the disturbances
445 from the historic gas production. When faults are moderately stressed, fluid-induced aseismic
446 creep can outpace the pressure diffusion front and trigger a seismicity front that propagates at

447 velocities that are orders of magnitude larger than the fluid diffusion (Bhattacharya and Viesca,
448 2019; Wynants-Morel *et al.*, 2020; Sáez *et al.*, 2022). Since these swarms are not driven directly
449 by stress changes from the industrial operations, they are not yet accounted for in induced
450 seismicity forecasting models for the Groningen gas field.

451

452 **Conclusions**

453 By applying a deep-learning-based workflow for earthquake detection to seismic data from the
454 Groningen gas field, we identify and locate a total of 1369 events from 2015 – 2022, almost two
455 times more than the standard KNMI catalog. Despite being automatically generated products, the
456 locations and magnitudes of the overlapping events display a high degree of similarity with the
457 KNMI catalog. Analysis of the nearest-neighbor distances reveals that the clusters account for 28%
458 of all events. Among the clustered events, approximately half are swarm-like clusters , while the
459 remaining half are aftershock-like clusters. The swarm-like clusters include five distinct swarm
460 sequences that migrate at incredibly fast velocities between 3 – 50 km/day along directions that do
461 not follow mapped faults or existing structures and frequently exhibit a sharp turn in the middle of
462 the sequence. Based on the observations of fast velocities and their depths in the Zechstein salt
463 above the reservoir caprock, the swarms are most likely not driven by fluids but rather other
464 aseismic processes such as propagating aseismic creep. The magnitude of these swarms is within
465 the detectable range of the KNMI catalog, but they were not previously identified. With a better
466 catalog, we can enhance our understanding of the mechanics of earthquake clusters and allow us
467 to better incorporate their contributions to seismic hazards into induced seismicity forecasting
468 models.

469 **References**

470 Acosta, M., J. Avouac, J. D. Smith, K. Sirorattanakul, H. Kaveh, and S. J. Bourne (2023). Earthquake Nucleation
471 Characteristics Revealed by Seismicity Response to Seasonal Stress Variations Induced by Gas Production
472 at Groningen, *Geophys. Res. Lett.* **50**, no. 19, e2023GL105455, doi: 10.1029/2023GL105455.

473 Ader, T. J., and J.-P. Avouac (2013). Detecting periodicities and declustering in earthquake catalogs using the
474 Schuster spectrum, application to Himalayan seismicity, *Earth Planet. Sci. Lett.* **377–378**, 97–105, doi:
475 10.1016/j.epsl.2013.06.032.

476 Ake, J., K. Mahrer, D. O'Connell, and L. Block (2005). Deep-Injection and Closely Monitored Induced Seismicity
477 at Paradox Valley, Colorado, *Bull. Seismol. Soc. Am.* **95**, no. 2, 664–683, doi: 10.1785/0120040072.

478 Albaric, J., V. Oye, N. Langet, M. Hasting, I. Lecomte, K. Iranpour, M. Messeiller, and P. Reid (2014). Monitoring
479 of induced seismicity during the first geothermal reservoir stimulation at Paralana, Australia, *Geothermics*
480 **52**, 120–131, doi: 10.1016/j.geothermics.2013.10.013.

481 Amezawa, Y., T. Maeda, and M. Kosuga (2021). Migration diffusivity as a controlling factor in the duration of
482 earthquake swarms, *Earth Planets Space* **73**, no. 1, 148, doi: 10.1186/s40623-021-01480-7.

483 Atkinson, G. M., D. W. Eaton, and N. Igonin (2020). Developments in understanding seismicity triggered by
484 hydraulic fracturing, *Nat. Rev. Earth Environ.* **1**, no. 5, 264–277, doi: 10.1038/s43017-020-0049-7.

485 Audin, L., J.-P. Avouac, M. Flouzat, and J.-L. Plantet (2002). Fluid-driven seismicity in a stable tectonic context:
486 The Remiremont fault zone, Vosges, France, *Geophys. Res. Lett.* **29**, no. 6, 13-1-13–4, doi:
487 10.1029/2001GL012988.

488 Baisie, M., and M. Paczuski (2004). Scale-free networks of earthquakes and aftershocks, *Phys. Rev. E* **69**, no. 6,
489 066106, doi: 10.1103/PhysRevE.69.066106.

490 Baisch, S., R. Weidler, R. Voros, D. Wyborn, and L. De Graaf (2006). Induced Seismicity during the Stimulation of
491 a Geothermal HFR Reservoir in the Cooper Basin, Australia, *Bulletin of the Seismological Society of*
492 *America* **96**, no. 6, 2242–2256, doi: 10.1785/0120050255.

493 Barnea Cohen, O., S. Cesca, T. Dahm, A. Hofstetter, Y. Hamiel, and A. Agnon (2022). Seismicity Induced at the
494 Northern Dead Sea Transform Fault, Kinneret (Sea of Galilee) Basin, by Shallow Creep Involving a Salt
495 Body, *Tectonics* **41**, no. 10, e2022TC007247, doi: 10.1029/2022TC007247.

496 Beyreuther, M., R. Barsch, L. Krischer, T. Megies, Y. Behr, and J. Wassermann (2010). ObsPy: A Python Toolbox
497 for Seismology, *Seismol. Res. Lett.* **81**, no. 3, 530–533, doi: 10.1785/gssrl.81.3.530.

498 Bhattacharya, P., and R. C. Viesca (2019). Fluid-induced aseismic fault slip outpaces pore-fluid migration, *Science*
499 **364**, no. 6439, 464–468, doi: 10.1126/science.aaw7354.

500 Bourne, S. J., and S. J. Oates (2017). Extreme threshold failures within a heterogeneous elastic thin sheet and the
501 spatial-temporal development of Induced seismicity within the Groningen gas field, *J. Geophys. Res. Solid*
502 *Earth* **122**, no. 12, 10,299–10,320, doi: 10.1002/2017JB014356.

503 Bourne, S. J., S. J. Oates, and J. van Elk (2018). The exponential rise of induced seismicity with increasing stress
504 levels in the Groningen gas field and its implications for controlling seismic risk, *Geophys. J. Int.* **213**, no.
505 3, 1693–1700, doi: 10.1093/gji/ggy084.

506 Bourne, S. J., S. J. Oates, J. Van Elk, and D. Doornhof (2014). A seismological model for earthquakes induced by
507 fluid extraction from a subsurface reservoir, *J. Geophys. Res. Solid Earth* **119**, no. 12, 8991–9015, doi:
508 10.1002/2014JB011663.

509 Buijze, L., P. A. J. Van Den Bogert, B. B. T. Wassing, B. Orlic, and J. Ten Veen (2017). Fault reactivation
510 mechanisms and dynamic rupture modelling of depletion-induced seismic events in a Rotliegend gas
511 reservoir, *Neth. J. Geosci.* **96**, no. 5, s131–s148, doi: 10.1017/njg.2017.27.

512 Burkitt, U., H. Van Oeveren, and P. Valvatne (2016). Groningen field review 2015 subsurface dynamic modelling
513 report, Nederlandse Aardolie Maatschappij.

514 Candela, T., S. Osinga, J. Ampuero, B. Wassing, M. Pluymaekers, P. A. Fokker, J. Wees, H. A. Waal, and A. G.
515 Muntendam-Bos (2019). Depletion-induced seismicity at the Groningen gas field: Coulomb rate-and-state
516 models including differential compaction effect, *J. Geophys. Res. Solid Earth* **124**, no. 7, 7081–7104, doi:
517 10.1029/2018JB016670.

518 Candela, T., M. Pluymaekers, J.-P. Ampuero, J.-D. van Wees, L. Buijze, B. Wassing, S. Osinga, N. Grobbe, and A.
519 G. Muntendam-Bos (2022). Controls on the spatio-temporal patterns of induced seismicity in Groningen
520 constrained by physics-based modelling with Ensemble-Smoother data assimilation, *Geophys. J. Int.* **229**,
521 no. 2, 1282–1308, doi: 10.1093/gji/ggab497.

522 Chen, X., and P. M. Shearer (2011). Comprehensive analysis of earthquake source spectra and swarms in the Salton
523 Trough, California, *J. Geophys. Res.* **116**, no. B9, B09309, doi: 10.1029/2011JB008263.

524 Clayton, P., G. Zalachoris, E. Rathje, T. Bheemasetti, S. Caballero, X. Yu, and S. Bennett (2016). The geotechnical
525 aspects of the September 3, 2016 M 5.8 Pawnee, Oklahoma earthquake, G69885, GEER Association,
526 Berkeley, California, 1–14 p.

527 Cochran, E. S., Z. E. Ross, R. M. Harrington, S. L. Dougherty, and J. L. Rubinstein (2018). Induced Earthquake
528 Families Reveal Distinctive Evolutionary Patterns Near Disposal Wells, *J. Geophys. Res. Solid Earth* **123**,
529 no. 9, 8045–8055, doi: 10.1029/2018JB016270.

530 Cochran, E. S., A. Wickham-Piotrowski, K. B. Kemna, R. M. Harrington, S. L. Dougherty, and A. F. Peña Castro
531 (2020). Minimal Clustering of Injection-Induced Earthquakes Observed with a Large-n Seismic Array,
532 *Bull. Seismol. Soc. Am.* **110**, no. 5, 2005–2017, doi: 10.1785/0120200101.

533 Dahm, T., and S. Hainzl (2022). A Coulomb Stress Response Model for Time-Dependent Earthquake Forecasts, *J.*
534 *Geophys. Res. Solid Earth* **127**, no. 9, e2022JB024443, doi: 10.1029/2022JB024443.

535 Danré, P., L. De Barros, F. Cappa, and J. Ampuero (2022). Prevalence of Aseismic Slip Linking Fluid Injection to
536 Natural and Anthropogenic Seismic Swarms, *J. Geophys. Res. Solid Earth* **127**, no. 12, e2022JB025571,
537 doi: 10.1029/2022JB025571.

538 Dempsey, D., and J. Suckale (2017). Physics-based forecasting of induced seismicity at Groningen gas field, the
539 Netherlands, *Geophys. Res. Lett.* **44**, no. 15, 7773–7782, doi: 10.1002/2017GL073878.

540 Dost, B., B. Edwards, and J. J. Bommer (2018). The Relationship between M and ML: A Review and Application to
541 Induced Seismicity in the Groningen Gas Field, The Netherlands, *Seismol. Res. Lett.* **89**, no. 3, 1062–1074,
542 doi: 10.1785/02201700247.

543 Dost, B., E. Ruigrok, and J. Spetzler (2017). Development of seismicity and probabilistic hazard assessment for the
544 Groningen gas field, *Neth. J. Geosci.* **96**, no. 5, s235–s245, doi: 10.1017/njg.2017.20.

545 Dublanchet, P., and L. De Barros (2021). Dual seismic migration velocities in seismic swarms, *Geophys. Res. Lett.*
546 **48**, no. 1, doi: 10.1029/2020GL090025.

547 Ellsworth, W. L. (2013). Injection-Induced Earthquakes, *Science* **341**, no. 6142, 1225942, doi:
548 10.1126/science.1225942.

549 van der Elst, N. J. (2021). *B-Positive* : A Robust Estimator of Aftershock Magnitude Distribution in Transiently
550 Incomplete Catalogs, *J. Geophys. Res. Solid Earth* **126**, no. 2, e2020JB021027, doi:
551 10.1029/2020JB021027.

552 Goebel, T. H. W., M. Weingarten, X. Chen, J. Haffner, and E. E. Brodsky (2017). The 2016 Mw5.1 Fairview,
553 Oklahoma earthquakes: Evidence for long-range poroelastic triggering at >40 km from fluid disposal wells,
554 *Earth Planet. Sci. Lett.* **472**, 50–61, doi: 10.1016/j.epsl.2017.05.011.

555 Grigoli, F., S. Cesca, E. Priolo, A. P. Rinaldi, J. F. Clinton, T. A. Stabile, B. Dost, M. G. Fernandez, S. Wiemer, and
556 T. Dahm (2017). Current challenges in monitoring, discrimination, and management of induced seismicity
557 related to underground industrial activities: A European perspective, *Rev. Geophys.* **55**, no. 2, 310–340, doi:
558 10.1002/2016RG000542.

559 Gualandi, A., C. Nichele, E. Serpelloni, L. Chiaraluce, L. Anderlini, D. Latorre, M. E. Belardinelli, and J.-P. Avouac
560 (2017). Aseismic deformation associated with an earthquake swarm in the northern Apennines (Italy),
561 *Geophys. Res. Lett.* **44**, no. 15, 7706–7714, doi: 10.1002/2017GL073687.

562 Hainzl, S., and T. Fischer (2002). Indications for a successively triggered rupture growth underlying the 2000
563 earthquake swarm in Vogtland/NW Bohemia, *J. Geophys. Res. Solid Earth* **107**, no. B12, ESE 5-1-ESE 5-
564 9, doi: 10.1029/2002JB001865.

565 Heimisson, E. R., J. D. Smith, J.-P. Avouac, and S. J. Bourne (2022). Coulomb threshold rate-and-state model for
566 fault reactivation: application to induced seismicity at Groningen, *Geophys. J. Int.* **228**, no. 3, 2061–2072,
567 doi: 10.1093/gji/ggab467.

568 Helmstetter, A., and D. Sornette (2002). Diffusion of epicenters of earthquake aftershocks, Omori's law, and
569 generalized continuous-time random walk models, *Phys. Rev. E* **66**, no. 6, 061104, doi:
570 10.1103/PhysRevE.66.061104.

571 Hicks, A. (2011). Clustering in multidimensional spaces with applications to statistical analysis of earthquake
572 clustering, University of Nevada, Reno.

573 Hough, S. E. (2015). Shaking intensity from injection-induced versus tectonic earthquakes in the central-eastern
574 United States, *Lead. Edge* **34**, no. 6, 690–697.

575 Hubbert, M. K., and W. W. Rubey (1959). Role of fluid pressure in mechanics of overthrust faulting, *Geol. Soc. Am.*
576 *Bull.* **70**, 115–166, doi: 10.1130/0016-7606(1959)70[115:ROFPIM]2.0.CO;2.

577 de Jager, J., and C. Visser (2017). Geology of the Groningen field – an overview, *Neth. J. Geosci.* **96**, no. 5, s3–s15,
578 doi: 10.1017/njg.2017.22.

579 Jiang, Y., S. V. Samsonov, and P. J. González (2022). Aseismic fault slip during a shallow normal-faulting seismic
580 swarm constrained using a physically informed geodetic inversion method, *J. Geophys. Res. Solid Earth*
581 **127**, no. 7, e2021JB022621, doi: 10.1029/2021JB022621.

582 Karimi, K., and J. Davidsen (2023). Separating Primary and Secondary Mechanisms for Seismicity Induced by
583 Hydraulic Fracturing, *Bull. Seismol. Soc. Am.* **113**, no. 5, 1982–1991, doi: 10.1785/0120220200.

584 Keranen, K. M., and M. Weingarten (2018). Induced Seismicity, *Annu. Rev. Earth Planet. Sci.* **46**, 149–174, doi:
585 10.1146/annurev-earth-082517-010054.

586 Kim, T., and J. Avouac (2023). Stress-Based and Convolutional Forecasting of Injection-Induced Seismicity:
587 Application to the Otaniemi Geothermal Reservoir Stimulation, *J. Geophys. Res. Solid Earth* **128**, no. 4,
588 e2022JB024960, doi: 10.1029/2022JB024960.

589 Kinscher, J., S. Cesca, P. Bernard, I. Contrucci, A. Mangeney, J. P. Piguet, and P. Bigarré (2016). Resolving source
590 mechanisms of microseismic swarms induced by solution mining, *Geophys. J. Int.* **206**, no. 1, 696–715,
591 doi: 10.1093/gji/ggw163.

592 Kühn, D., S. Hainzl, T. Dahm, G. Richter, and I. Vera Rodriguez (2022). A review of source models to further the
593 understanding of the seismicity of the Groningen field, *Neth. J. Geosci.* **101**, e11, doi: 10.1017/njg.2022.7.

594 Kwiatek, G., T. Saarno, T. Ader, F. Bluemle, M. Bohnhoff, M. Chendorain, G. Dresen, P. Heikkinen, I. Kukkonen,
595 P. Leary, *et al.* (2019). Controlling fluid-induced seismicity during a 6.1-km-deep geothermal stimulation
596 in Finland, *Sci. Adv.* **5**, no. 5, eaav7224, doi: 10.1126/sciadv.aav7224.

597 Langenbruch, C., M. Weingarten, and M. D. Zoback (2018). Physics-based forecasting of man-made earthquake
598 hazards in Oklahoma and Kansas, *Nat. Commun.* **9**, 3946, doi: 10.1038/s41467-018-06167-4.

599 Lei, X., Z. Wang, and J. Su (2019). Possible link between long-term and short-term water injections and earthquakes
600 in salt mine and shale gas site in Changning, south Sichuan Basin, China, *Earth Planet. Phys.* **3**, no. 6, 510–
601 525, doi: 10.26464/epp2019052.

602 Lohman, R. B., and J. J. McGuire (2007). Earthquake swarms driven by aseismic creep in the Salton Trough,
603 California, *J. Geophys. Res.* **112**, no. B4, B04405, doi: 10.1029/2006JB004596.

604 Martínez-Garzón, P., I. Zaliapin, Y. Ben-Zion, G. Kwiatek, and M. Bohnhoff (2018). Comparative Study of
605 Earthquake Clustering in Relation to Hydraulic Activities at Geothermal Fields in California, *J. Geophys.
606 Res. Solid Earth* **123**, 4041–4062, doi: 10.1029/2017JB014972.

607 Meyer, H., J. D. Smith, S. Bourne, and J.-P. Avouac (2023). An integrated framework for surface deformation
608 modelling and induced seismicity forecasting due to reservoir operations, *Geol. Soc. Spec. Publ.* **528**, no. 1,
609 299–318, doi: 10.1144/SP528-2022-169.

610 Moein, M. J. A., C. Langenbruch, R. Schultz, F. Grigoli, W. L. Ellsworth, R. Wang, A. P. Rinaldi, and S. Shapiro
611 (2023). The physical mechanisms of induced earthquakes, *Nat. Rev. Earth Environ.* **4**, no. 12, 847–863,
612 doi: 10.1038/s43017-023-00497-8.

613 Mogi, K. (1963). Some discussions on aftershocks, foreshocks and earthquake swarms—The fracture of a semi-
614 infinite body caused by an inner stress origin and its relation to the earthquake phenomena (3rd paper),
615 *Bull. Earthquake Res. Inst. Univ. Tokyo* **41**, no. 3, 615–658.

616 Muntendam-Bos, A. G. (2020). Clustering characteristics of gas-extraction induced seismicity in the Groningen gas
617 field, *Geophys. J. Int.* **221**, no. 2, 879–892, doi: 10.1093/gji/ggaa038.

618 Muntendam-Bos, A. G., J. P. A. Roest, and H. A. De Waal (2017). The effect of imposed production measures on
619 gas extraction induced seismic risk, *Neth. J. Geosci.* **96**, no. 5, s271–s278, doi: 10.1017/njg.2017.29.

620 Nederlandse Aardolie Maatschappij (2017). Groningen Velocity Model 2017 - Groningen full elastic velocity model
621 September 2017.

622 NORSAR (2018). Review of the public KNM induced earthquake catalogue from the Groningen gas field, Project
623 Phase 1, WP1.

624 Nur, A., and J. R. Booker (1972). Aftershocks caused by pore fluid flow?, *Science* **175**, no. 4024, 885–887, doi:
625 10.1126/science.175.4024.885.

626 Oates, S., A. J. Landman, O. van der Wal, H. Baehr, and H. Piening (2022). Geomechanical, seismological, and
627 geodetic data pertaining to the Groningen gas field: a data package used in the “Mmax II Workshop”, on
628 constraining the maximum earthquake magnitude in the Groningen field, Utrecht University, doi:
629 10.24416/UU01-RHHRPY.

630 Ogata, Y. (1988). Statistical models for earthquake occurrences and residual analysis for point processes, *J. Am.*
631 *Stat. Assoc.* **83**, no. 401, 9–27.

632 Omori, F. (1894). On the aftershocks of earthquakes, *J. Coll. Sci. Imp. Univ. Tokyo* **7**, 111–200.

633 Park, Y., S. M. Mousavi, W. Zhu, W. L. Ellsworth, and G. C. Beroza (2020). Machine-Learning-Based Analysis of
634 the Guy-Greenbrier, Arkansas Earthquakes: A Tale of Two Sequences, *Geophys. Res. Lett.* **47**, no. 6,
635 e2020GL087032, doi: 10.1029/2020GL087032.

636 Passarelli, L., S. Hainzl, S. Cesca, F. Maccaferri, M. Mucciarelli, D. Roessler, F. Corbi, T. Dahm, and E. Rivalta
637 (2015). Aseismic transient driving the swarm-like seismic sequence in the Pollino range, Southern Italy,
638 *Geophys. J. Int.* **201**, no. 3, 1553–1567, doi: 10.1093/gji/ggv111.

639 Post, R. A. J., M. A. J. Michels, J.-P. Ampuero, T. Candela, P. A. Fokker, J.-D. Van Wees, R. W. V. D. Hofstad, and
640 E. R. V. D. Heuvel (2021). Interevent-time distribution and aftershock frequency in non-stationary induced
641 seismicity, *Sci. Rep.* **11**, no. 1, 3540, doi: 10.1038/s41598-021-82803-2.

642 Richter, C. (1958). *Elementary Seismology*, W. H. Freeman and Co, San Francisco.

643 Richter, G., S. Hainzl, T. Dahm, and G. Zöller (2020). Stress-based, statistical modeling of the induced seismicity at
644 the Groningen gas field, The Netherlands, *Environ. Earth Sci.* **79**, no. 11, 252, doi: 10.1007/s12665-020-
645 08941-4.

646 Ross, Z. E., and E. S. Cochran (2021). Evidence for latent crustal fluid injection transients in Southern California
647 from long-duration earthquake swarms, *Geophys. Res. Lett.* **48**, no. 12, doi: 10.1029/2021GL092465.

648 Ruhl, C. J., R. E. Abercrombie, K. D. Smith, and I. Zaliapin (2016). Complex spatiotemporal evolution of the 2008
649 M_w 4.9 Mogul earthquake swarm (Reno, Nevada): Interplay of fluid and faulting, *J. Geophys. Res. Solid*
650 *Earth* **121**, no. 11, 8196–8216, doi: 10.1002/2016JB013399.

651 Sáez, A., B. Lecampion, P. Bhattacharya, and R. C. Viesca (2022). Three-dimensional fluid-driven stable frictional
652 ruptures, *Journal of the Mechanics and Physics of Solids* **160**, 104754, doi: 10.1016/j.jmps.2021.104754.

653 Schoenball, M., N. C. Davatzes, and J. M. G. Glen (2015). Differentiating induced and natural seismicity using
654 space-time-magnitude statistics applied to the Coso Geothermal field, *Geophys. Res. Lett.* **42**, no. 15, 6221–
655 6228, doi: 10.1002/2015GL064772.

656 Schuster, A. (1897). On lunar and solar periodicities of earthquakes, *Proc. R. Soc. Lond.* **61**, 455–465.

657 Segall, P. (1989). Earthquakes triggered by fluid extraction, *Geology* **17**, 942–946.

658 Segall, P., J. Grasso, and A. Mossop (1994). Poroelastic stressing and induced seismicity near the Lacq gas field,
659 southwestern France, *J. Geophys. Res.* **99**, no. B8, 15423–15438, doi: 10.1029/94JB00989.

660 Segall, P., and S. Lu (2015). Injection-induced seismicity: Poroelastic and earthquake nucleation effects, *JGR Solid*
661 *Earth* **120**, no. 7, 5082–5103, doi: 10.1002/2015JB012060.

662 Shapiro, S. A., E. Huenges, and G. Borm (1997). Estimating the crust permeability from fluid-injection-induced
663 seismic emission at the KTB site, *Geophys. J. Int.* **131**, no. 2, F15–F18, doi: 10.1111/j.1365-
664 246X.1997.tb01215.x.

665 Shelly, D. R., S. C. Moran, and W. A. Thelen (2013). Evidence for fluid-triggered slip in the 2009 Mount Rainier,
666 Washington earthquake swarm, *Geophys. Res. Lett.* **40**, no. 8, 1506–1512, doi: 10.1002/grl.50354.

667 Sirorattanakul, K., Z. E. Ross, M. Khoshmanesh, E. S. Cochran, M. Acosta, and J. Avouac (2022). The 2020
668 Westmorland, California Earthquake Swarm as Aftershocks of a Slow Slip Event Sustained by Fluid Flow,
669 *J. Geophys. Res. Solid Earth* **127**, no. 11, e2022JB024693, doi: 10.1029/2022JB024693.

670 Smith, J. D., J. Avouac, R. S. White, A. Copley, A. Gualandi, and S. Bourne (2019). Reconciling the Long-Term
671 Relationship Between Reservoir Pore Pressure Depletion and Compaction in the Groningen Region, *J.
672 Geophys. Res. Solid Earth* **124**, no. 6, 6165–6178, doi: 10.1029/2018JB016801.

673 Smith, J. D., E. R. Heimisson, S. J. Bourne, and J.-P. Avouac (2022). Stress-based forecasting of induced seismicity
674 with instantaneous earthquake failure functions: Applications to the Groningen gas reservoir, *Earth Planet.
675 Sci. Lett.* **594**, 117697, doi: 10.1016/j.epsl.2022.117697.

676 Smith, J. D., Z. E. Ross, K. Azizzadenesheli, and J. B. Muir (2021). HypoSVI: Hypocentre inversion with Stein
677 variational inference and physics informed neural networks, *Geophysical Journal International* **228**, no. 1,
678 698–710, doi: 10.1093/gji/ggab309.

679 Smith, J. D., R. S. White, J.-P. Avouac, and S. Bourne (2020). Probabilistic earthquake locations of induced
680 seismicity in the Groningen region, the Netherlands, *Geophys. J. Int.* **222**, no. 1, 507–516, doi:
681 10.1093/gji/ggaa179.

682 Spetzler, J., and B. Dost (2017). Hypocentre estimation of induced earthquakes in Groningen, *Geophys. J. Int.* **209**,
683 453–465, doi: 10.1093/gji/ggx020.

684 Stäuble, A. J., and G. Milius (1970). Geology of Groningen Gas Field, Netherlands, in *Geology of Giant Petroleum
685 Fields* M. Halbouty(Editor), American Association of Petroleum Geologists, 359–369.

686 Tan, Y. J., F. Waldhauser, W. L. Ellsworth, M. Zhang, W. Zhu, M. Michele, L. Chiaraluce, G. C. Beroza, and M.
687 Segou (2021). Machine-Learning-Based High-Resolution Earthquake Catalog Reveals How Complex Fault
688 Structures Were Activated during the 2016–2017 Central Italy Sequence, *Seism. rec.* **1**, no. 1, 11–19, doi:
689 10.1785/0320210001.

690 van Thienen-Visser, K., and J. Breunese (2015). Induced seismicity of the Groningen gas field: History and recent
691 developments, *Lead. Edge* **34**, no. 6, 664–671, doi: 10.1190/tle34060664.1.

692 Trampert, J., R. Benzi, and F. Toschi (2022). Implications of the statistics of seismicity recorded within the
693 Groningen gas field, *Neth. J. Geosci.* **101**, e9, doi: 10.1017/njg.2022.8.

694 Trugman, D. T., P. M. Shearer, A. A. Borsa, and Y. Fialko (2016). A comparison of long-term changes in seismicity
695 at The Geysers, Salton Sea, and Coso geothermal fields, *J. Geophys. Res. Solid Earth* **121**, 225–247, doi:
696 10.1002/2015JB012510.

697 Utsu, T. (1961). A statistical study on the occurrence of aftershocks, *The Geophysical Magazine* **30**, 521–605.

698 Van Wees, J.-D., S. Osinga, K. Van Thienen-Visser, and P. A. Fokker (2018). Reservoir creep and induced
699 seismicity: inferences from geomechanical modeling of gas depletion in the Groningen field, *Geophys. J.
700 Int.* **212**, no. 3, 1487–1497, doi: 10.1093/gji/ggx452.

701 Visser, C. A., and J. L. Solano Viota (2017). Introduction to the Groningen static reservoir model, *Neth. J. Geosci.*
702 **96**, no. 5, s39–s46, doi: 10.1017/njg.2017.25.

703 de Waal, J. A., A. G. Muntendam-Bos, and J. P. A. Roest (2015). Production induced subsidence and seismicity in
704 the Groningen gas field – can it be managed?, *Proc. Int. Assoc. Hydrol. Sci.* **372**, 129–139, doi:
705 10.5194/piahs-372-129-2015.

706 Wiemer, S., and M. Wyss (2000). Minimum magnitude of completeness in earthquake catalogs: Examples from
707 Alaska, the Western United States, and Japan, *Bulletin of the Seismological Society of America* **90**, no. 4,
708 859–869, doi: 10.1785/0119990114.

709 Wilding, J. D., W. Zhu, Z. E. Ross, and J. M. Jackson (2023). The magmatic web beneath Hawai‘i, *Science* **379**, no.
710 6631, 462–468, doi: 10.1126/science.ade5755.

711 Willacy, C., E. Van Dedem, S. Minisini, J. Li, J.-W. Blokland, I. Das, and A. Droujinine (2019). Full-waveform
712 event location and moment tensor inversion for induced seismicity, *Geophysics* **84**, no. 2, KS39–KS57, doi:
713 10.1190/geo2018-0212.1.

714 Woessner, J., and S. Wiemer (2005). Assessing the quality of earthquake catalogues: Estimating the magnitude of
715 completeness and its uncertainty, *Bulletin of the Seismological Society of America* **95**, no. 2, 684–698, doi:
716 10.1785/0120040007.

717 Wu, W., D. Lu, and D. Elsworth (2022). Fluid injection-induced fault slip during unconventional energy
718 development: A review, *Energy Reviews* **1**, no. 2, 100007, doi: 10.1016/j.enrev.2022.100007.

719 Wynants-Morel, N., F. Cappa, L. De Barros, and J.-P. Ampuero (2020). Stress Perturbation From Aseismic Slip
720 Drives the Seismic Front During Fluid Injection in a Permeable Fault, *J. Geophys. Res. Solid Earth* **125**,
721 e2019JB01979, doi: 10.1029/2019JB019179.

722 Yukutake, Y., K. Yoshida, and R. Honda (2022). Interaction between aseismic slip and fluid invasion in earthquake
723 swarms revealed by dense geodetic and seismic observations, *J. Geophys. Res. Solid Earth*, doi:
724 10.1029/2021JB022933.

725 Zaliapin, I., and Y. Ben-Zion (2016). Discriminating Characteristics of Tectonic and Human-Induced Seismicity,
726 *Bulletin of the Seismological Society of America* **106**, no. 3, 846–859, doi: 10.1785/0120150211.

727 Zaliapin, I., and Y. Ben-Zion (2013a). Earthquake clusters in southern California I: Identification and stability, *J.*
728 *Geophys. Res. Solid Earth* **118**, no. 6, 2847–2864, doi: 10.1002/jgrb.50179.

729 Zaliapin, I., and Y. Ben-Zion (2013b). Earthquake clusters in southern California II: Classification and relation to
730 physical properties of the crust, *J. Geophys. Res. Solid Earth* **118**, no. 6, 2865–2877, doi:
731 10.1002/jgrb.50178.

732 Zaliapin, I., and Y. Ben-Zion (2020). Earthquake declustering using the nearest-neighbor approach in space-time-
733 magnitude domain, *J. Geophys. Res. Solid Earth* **125**, no. 4, doi: 10.1029/2018JB017120.

734 Zaliapin, I., A. Gabrielov, V. Keilis-Borok, and H. Wong (2008). Clustering analysis of seismicity and aftershock
735 identification, *Phys. Rev. Lett.* **101**, no. 1, 018501, doi: 10.1103/PhysRevLett.101.018501.

736 Zhai, G., M. Shirzaei, M. Manga, and X. Chen (2019). Pore-pressure diffusion, enhanced by poroelastic stresses,
737 controls induced seismicity in Oklahoma, *Proc Natl Acad Sci USA* **116**, no. 33, 16228–16233, doi:
738 10.1073/pnas.1819225116.

739 Zhu, W., and G. C. Beroza (2019). PhaseNet: A Deep-Neural-Network-Based Seismic Arrival Time Picking
740 Method, *Geophys. J. Int.*, doi: 10.1093/gji/ggy423.

741 Zhu, W., I. W. McBrearty, S. M. Mousavi, W. L. Ellsworth, and G. C. Beroza (2022). Earthquake Phase Association
742 Using a Bayesian Gaussian Mixture Model, *JGR Solid Earth* **127**, no. 5, e2021JB023249, doi:
743 10.1029/2021JB023249.

744

745 **Data and Resources**

746 Raw seismic waveforms were accessed through the ORFEUS (Observatories and Research
747 Facilities for European Seismology) FDSN (International Federation of Digital Seismograph
748 Networks) client via a python script using the package Obspy (<https://docs.obspy.org/>; Beyreuther
749 *et al.*, 2010). 3D seismic velocity and faults map were provided to us by Shell Global Solutions
750 International B.V. Computer programs used to generate the enhanced seismicity catalog are
751 previously published and can be found in the following references: seismic phase detection
752 software PhaseNet (<https://github.com/AI4EPS/PhaseNet>; Zhu and Beroza, 2019), seismic phase
753 association software GaMMA (<https://github.com/AI4EPS/GaMMA>; Zhu *et al.*, 2022),
754 hypocenter inversion software HypoSVI (<https://github.com/Ulvetanna/HypoSVI>; Smith
755 *et al.*, 2021). The seismicity catalog from the Royal Netherland Meteorological Survey (KNMI) is
756 available online at www.knmi.nl. Matlab version 2020a were used to analyze data and prepare
757 figures. The enhanced seismicity catalog generated in this study along with the picks of arrival
758 times and codes used to analyze them are made available online at CaltechDATA repository (links
759 will be provided after revisions).

760

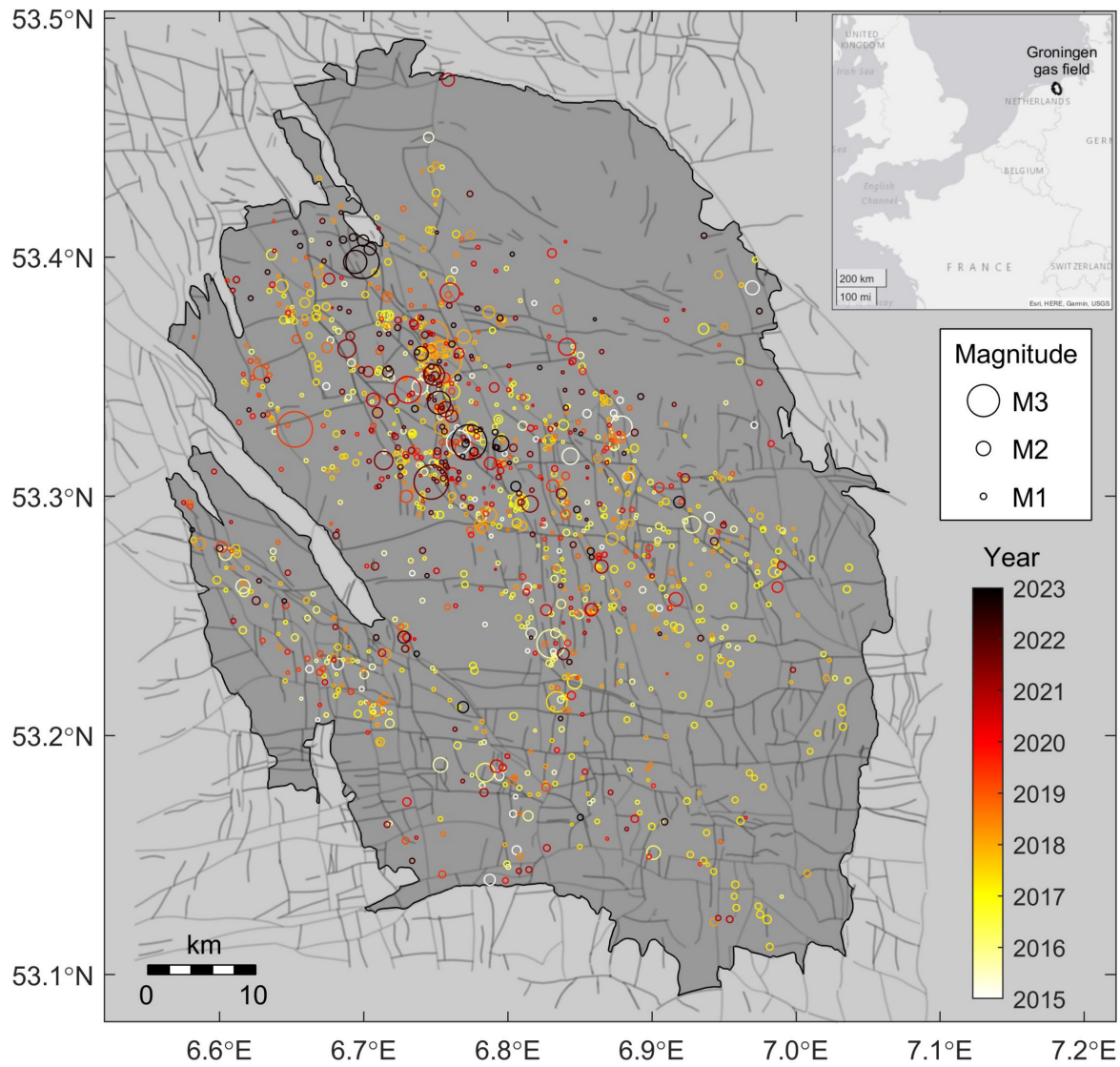
761 **Declaration of Competing Interests**

762 The authors acknowledge that there are no conflicts of interest available.

763

764 **Acknowledgements**

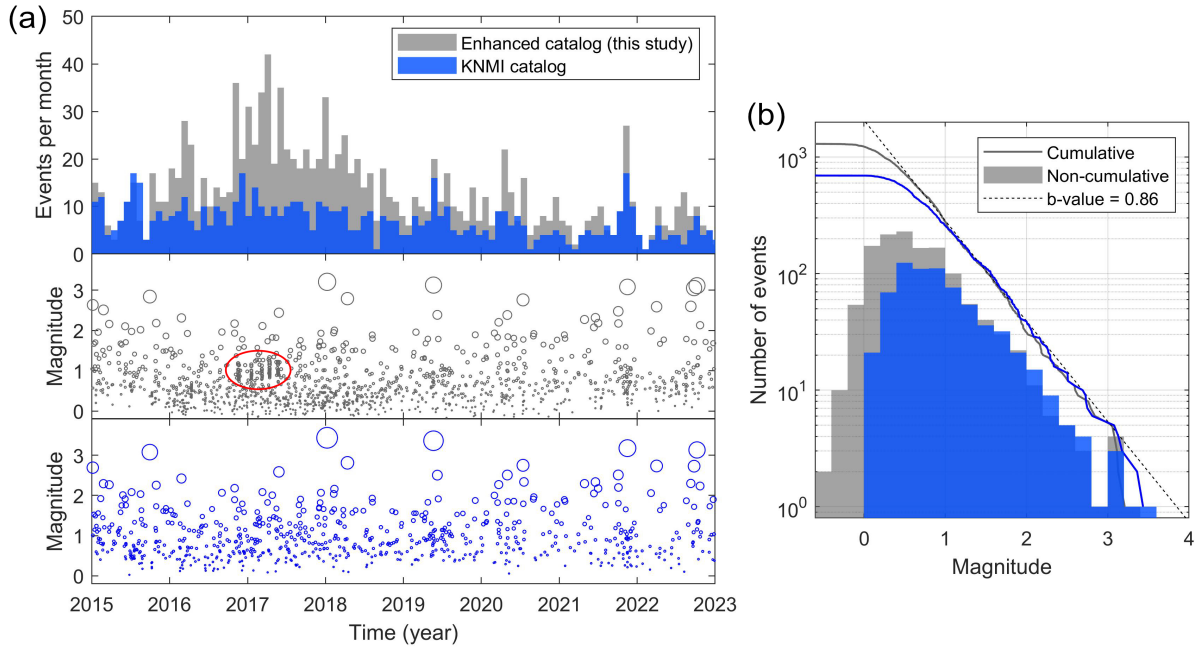
765 This research is supported by the NSF/Industry-University Collaborative Research Center
766 “Geomechanics and Mitigation of Geohazards” (National Science Foundation award #1822214),
767 and the Enhancement Project GMG-3 funded by Nederlandse Aardolie Maatschappij (NAM). We
768 gratefully acknowledge data and support from Shell Global Solutions and thank editor Allison
769 Bent, the associate editor, and two anonymous reviewers for insightful and detailed comments,
770 which greatly improved the quality of the manuscript.



771

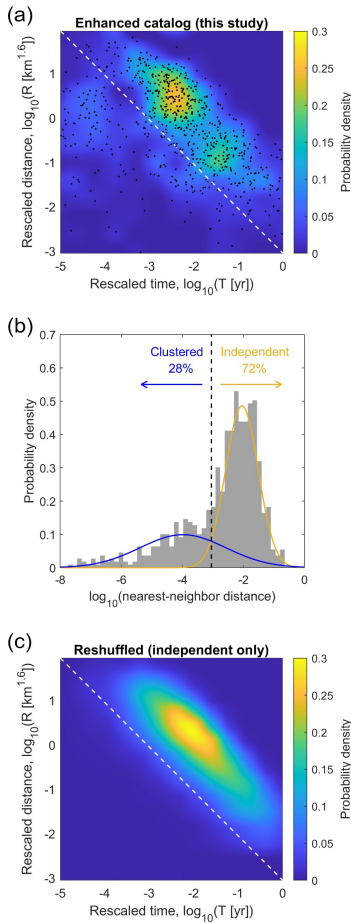
772 **Figure 1.** Map of induced seismicity in the Groningen gas field from 2015 – 2023 that were
773 detected and located in this study using a deep-learning-based workflow. Circles show events with
774 size representing the local magnitude and color representing the occurrence time. Black line shows
775 the outline of the reservoir. Gray lines show mapped faults. The inset shows the location of the gas
776 field within Europe.

777



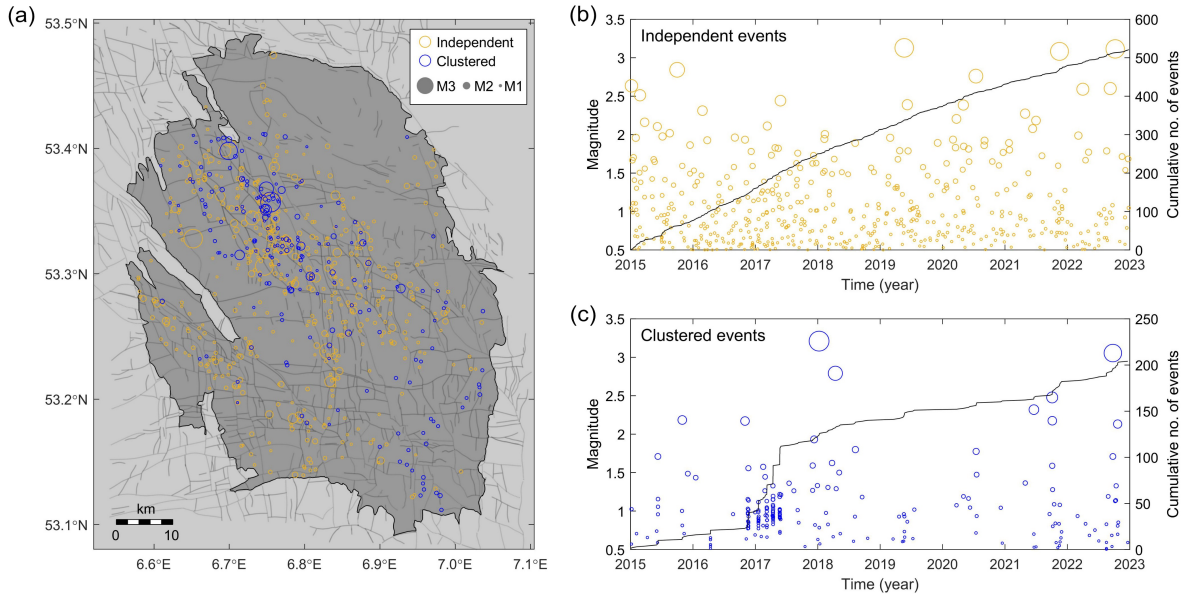
778

779 **Figure 2.** Enhanced seismicity catalog. (a) Comparison between our enhanced seismicity catalog
780 and the standard catalog from the Royal Netherlands Meteorological Institute (KNMI). The top
781 panel compares number of detected events per month. The middle panel shows distribution of
782 event magnitude vs. time for the enhanced catalog. The red circle highlights the five newly
783 detected swarm sequences. The bottom panel is the same as the middle but for the KNMI catalog.
784 (b) Frequency-magnitude distribution from the two catalogs. The dashed line represents the
785 Gutenberg-Richter exponential distribution with the b-value slope of 0.86 estimated from the
786 enhanced catalog using B-Positive method (van der Elst, 2021). The completeness magnitude (M_c)
787 of the enhanced catalog is estimated to be approximately 0.5.



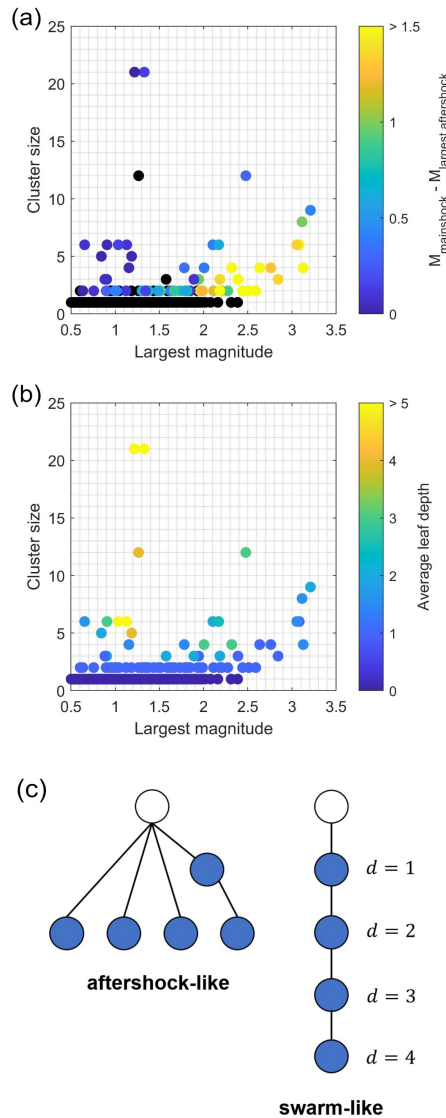
788

789 **Figure 3.** Nearest-neighbor clustering analysis performed on our enhanced seismicity catalog with
 790 $M_L \geq 0.5$. Only epicenters are used and the fractal dimension (d_f) is taken to be 1.6. (a) A joint
 791 2-D distribution of the rescaled time and rescaled distance. Each of the black dots represent
 792 proximity of each event to a parent event. (b) Histogram of the nearest-neighbor proximity distance
 793 with curves showing the two Gaussian distributions representing the two modes derived from 1-D
 794 Gaussian mixture model. (c) The average joint distribution of the rescaled time and rescaled
 795 distance derived from 100 catalogs created from reshuffling locations and magnitudes of
 796 independent events. The diagonal white dashed lines in panels (a) and (c) and black vertical dashed
 797 line in panel (b) mark the mode separator ($\eta_0 = 10^{-3.05}$) used to perform binary classification of
 798 events into either independent or clustered.



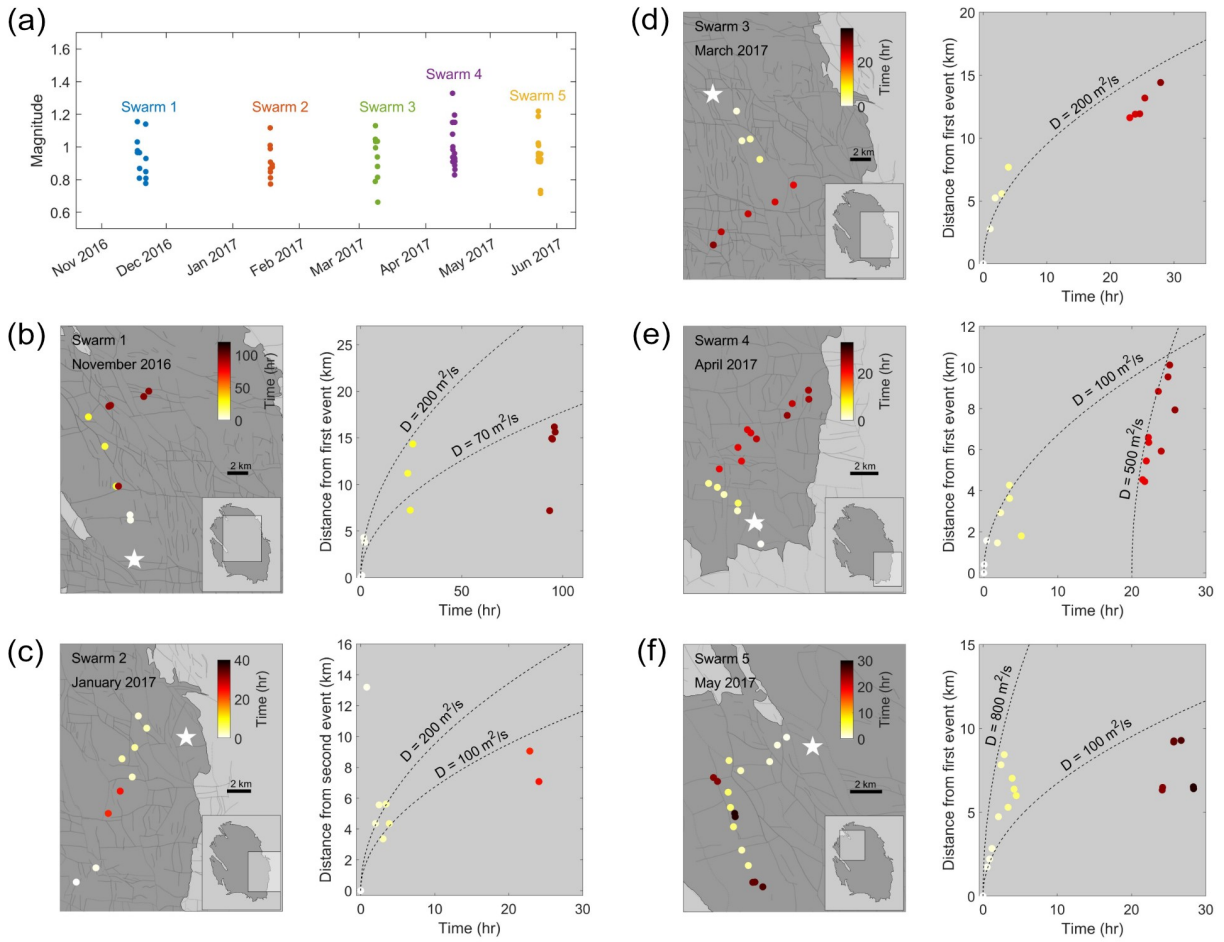
799

800 **Figure 4.** Distribution of independent vs. clustered events for $M_L \geq 0.5$ from our enhanced
801 seismicity catalog. (a) Spatial distribution of events color coded by the mode they belong to. (b)
802 Magnitude and cumulative number of events vs. time distribution of the independent events. (c)
803 Same as (b) but for clustered events.



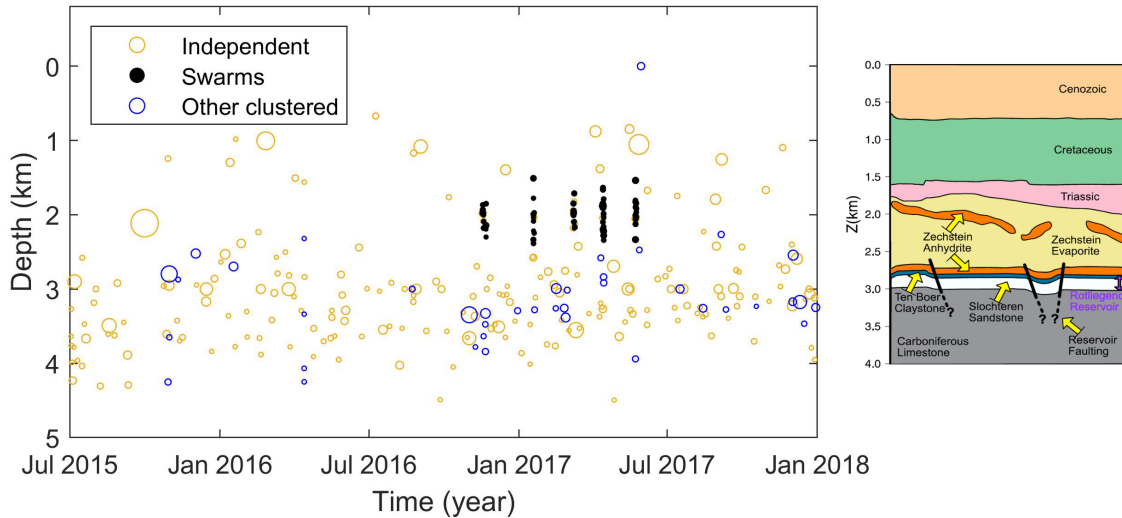
804

805 **Figure 5.** Statistics of the identified clusters. (a) Cluster size (number of events) vs. magnitude of
 806 the largest event color coded by the magnitude difference between mainshock and largest
 807 aftershock. Black circles denote the case with only one event in the cluster or when the largest
 808 earthquake is the last one in the sequence. (b) is the same as (a) but color coded by the average
 809 leaf depth. (c) A schematic showing aftershock-like and swarm-like sequences. Aftershock-like
 810 sequence has smaller average leaf depth than swarm-like sequence, but each event produces more
 811 offsprings.



812

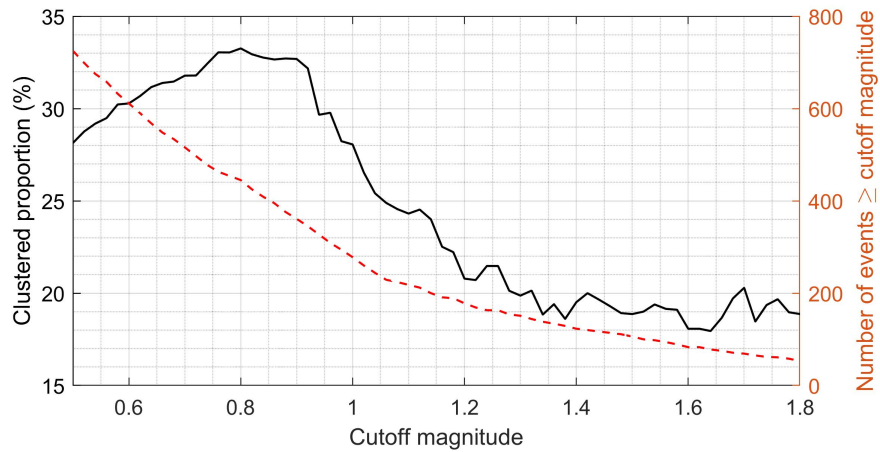
813 **Figure 6.** Fast propagating earthquake swarms. (a) Magnitude vs. time of the five distinct bursts
 814 of swarm-like sequences. (b) – (f) show the spatiotemporal evolution of these five swarms. The
 815 white stars mark the second event in swarm 2 and first event in all other swarms. The dashed lines
 816 show the predicted expansion for the different values of apparent hydraulic diffusivity D .



817

818 **Figure 7.** Depth distribution of earthquakes with $M_L \geq 0.5$ from our enhanced seismicity catalog
819 with colors identifying whether they are independent, fast propagating swarms shown in Figure 6,
820 or other clustered events, along with a schematic showing a depth cross-section of lithologies taken
821 from Smith et al. (2019). Only the time period where we have picks from both surface and borehole
822 sensors are shown. The five swarm sequences are located in the Zechstein evaporite.

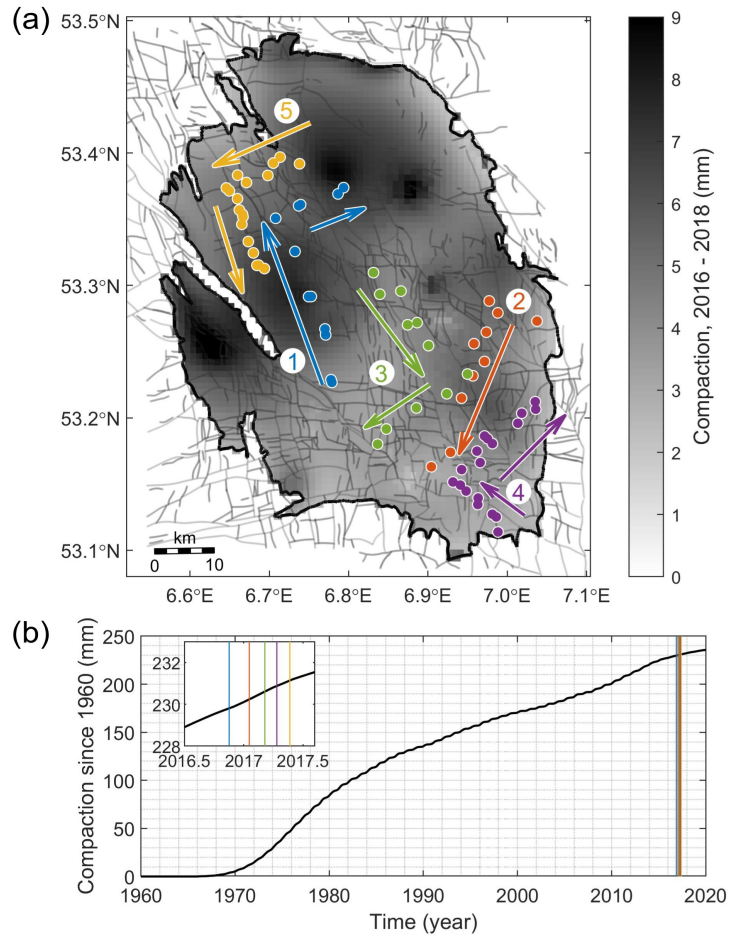
823



824

825 **Figure 8.** Variations of clustered proportion for the different cutoff magnitude. The dashed line
826 shows the number of events larger than or equal to a given cutoff magnitude.

827



828

829 **Figure 9.** Comparison of swarms with reservoir compaction. (a) Spatial distribution of modelled
830 reservoir compaction between 2016 and 2018. The calculation is done using a simple expression
831 $C = C_m \cdot \Delta P \cdot h$ relating compaction C with the compressibility C_m from Smith *et al.* (2019)
832 constrained with geodetic data, pressure depletion ΔP from Acosta *et al.* (2023) calculated using
833 a simplified reservoir model from Meyer *et al.* (2023) constrained with pressure measurements
834 from the borehole sensors, and the reservoir thickness h . The circles with different colors denote
835 the five different swarms shown in Figure 6. (b) Average compaction in the reservoir vs. time. The
836 vertical lines denote the timing of the five swarms. The inset shows a zoomed-in during the time
837 of swarms.

838 **Table 1.** A compilation of clustered fraction of seismicity from different regions. With the
839 exception of Post *et al.* (2021), which utilizes the statistics of interevent times, all other studies
840 utilized the nearest-neighbor distance approach (Zaliapin *et al.*, 2008; Zaliapin and Ben-Zion,
841 2013a).

Region	Type of seismicity	Magnitude cutoff	Clustered fraction
Southern California (Zaliapin and Ben-Zion, 2013a)	Mostly tectonic	2	0.70
San Jacinto fault zone, California, USA (Zaliapin and Ben-Zion, 2016)	Tectonic	1	0.34
Coso geothermal field, California, USA (Zaliapin and Ben-Zion, 2016)	Mixed	1	0.44
Salton Sea geothermal field, California, USA (Zaliapin and Ben-Zion, 2016)	Mixed	1.5	0.69
Geysers geothermal field, California, USA (Zaliapin and Ben-Zion, 2016)	Induced	1.0	0.17
TauTona gold mine, South Africa (Zaliapin and Ben-Zion, 2016)	Induced	1.5	0.12
Saltwater disposal, Oklahoma (Cochran <i>et al.</i> , 2020)	Induced	0.95	0.30
Hydraulic fracturing in western Alberta, Canada (Karimi and Davidsen, 2023)	Induced	0.2	0.25

Groningen gas field, Netherlands, KNMI catalog (Candela <i>et al.</i> , 2019)	Induced	1.0	0.18
Groningen gas field, Netherlands, KNMI catalog (Post <i>et al.</i> , 2021)	Induced	1.3	0.27
Groningen gas field, Netherlands, KNMI catalog between 01/1995 – 01/2019 (Muntendam-Bos, 2020)	Induced	1.2	0.06
Groningen gas field, Netherlands, KNMI catalog between 05/2014 – 01/2019 (Muntendam-Bos, 2020)	Induced	1.2	0.22
Groningen gas field, Netherlands, enhanced catalog (this study)	Induced	0.5	0.28
Groningen gas field, Netherlands, enhanced catalog (this study)	Induced	1.2	0.21